

Center for Advanced Materials

# CAM

Presented at the American Welding Society,  
69th Annual Convention, New Orleans, LA,  
April 17-22, 1988

## High-Mn Steel Weldment Mechanical Properties at 4 K

J.W. Chan, A.J. Sunwoo, and J.W. Morris, Jr.

June 1988

REPRODUCED FROM  
BEST AVAILABLE COPY



**Materials and Chemical Sciences Division**

**Lawrence Berkeley Laboratory • University of California**

ONE CYCLOTRON ROAD, BERKELEY, CA 94720 • (415) 486-4755

## DISCLAIMER

LBL--25023

DE88 013599

This report was prepared as an account of work sponsored by an agency of the United States Government. Neither the United States Government nor any agency thereof, nor any of their employees, makes any warranty, express or implied, or assumes any legal liability or responsibility for the accuracy, completeness, or usefulness of any information, apparatus, product, or process disclosed, or represents that its use would not infringe privately owned rights. Reference herein to any specific commercial product, process, or service by trade name, trademark, manufacturer, or otherwise does not necessarily constitute or imply its endorsement, recommendation, or favoring by the United States Government or any agency thereof. The views and opinions of authors expressed herein do not necessarily state or reflect those of the United States Government or any agency thereof.

## High-Mn Steel Weldment Mechanical Properties at 4 K

J. W. Chan, A. J. Sunwoo and J. W. Morris, Jr.

Center for Advanced Materials  
Materials and Chemical Sciences Division  
Lawrence Berkeley Laboratory  
University of California

and

Department of Materials Science and Mineral Engineering  
University of California at Berkeley  
Berkeley, California 94720

June 1988

This work is supported by the Director, Office of Energy Research,  
Office of Fusion Energy, Development and Technology Division of the  
U. S. Department of Energy under Contract No. DE-AC03-76SF00098

MASTER

# High-Mn Steel Weldment Mechanical Properties at 4 K

J. W. Chan, A. J. Sunwoo, and J. W. Morris, Jr.

Center for Advanced Materials  
Lawrence Berkeley Laboratory  
and

Department of Materials Science & Mineral Engineering  
University of California, Berkeley

Advanced high-field superconducting magnets of the next generation of magnetic confinement fusion devices will require structural alloys with high yield strength and high toughness at cryogenic temperatures. Commercially available alloys used in the current generation of magnets, such as 300 series stainless steels, do not have the required properties. N-strengthened, high-Mn alloys meet base plate requirements in the as-rolled condition. However, the property changes associated with weld microstructural and chemical changes in these alloys have not been well characterized. In this work welding induced cryogenic mechanical property changes of an 18Mn-16Cr-5Ni-0.2N alloy are correlated with as-solidified weld microstructures and chemistries.

## INTRODUCTION

Commercially viable fusion reactors require high field superconducting magnets for plasma confinement. Various design considerations impose severe requirements on the cryogenic mechanical properties of alloys used as structural materials in these magnets. Projected requirements as proposed by JAERI (Japan Atomic Energy Research Institute) for their next experimental reactor, for example, are 1200 MPa yield strength and 200 MPa-m<sup>1/2</sup> K<sub>IC</sub> for the base material [1] at 4.2K and 1000 MPa yield strength and 200 MPa-m<sup>1/2</sup> K<sub>IC</sub> for weldments [2]. The U. S. goals [3-4], based on the best achievable properties of current commercially available austenitic alloys, are 1000 MPa yield and 200 MPa-m<sup>1/2</sup> K<sub>IC</sub> for the base metal with minimum properties of 1000 MPa yield and 150 MPa-m<sup>1/2</sup> K<sub>IC</sub> in the welded condition.

The alloy classes considered for this application are the nitrogen-strengthened austenitic Fe-Cr-Ni alloys and the more recently developed nitrogen-strengthened austenitic Fe-Mn-Cr-Ni alloys [3]. The mechanical properties of best current commercially available austenitic Fe-Cr-Ni alloys can satisfy U.S. goals for base metal but cannot meet the JAERI goals in either the welded or base conditions. N-strengthened high-Mn austenitic alloys appear a more promising alternative. In particular an alloy of nominal composition 18Mn-5Ni-16Cr-0.22N, has been able to approach the Japanese goals for base metal properties [5] with proper thermomechanical processing (TMP). Work on a 22Mn-13Cr-5Ni-0.2N alloy has shown that it can satisfy the

base metal properties goals in heavy sections with proper TMP [6]. The weldability of these alloys has not been examined in detail.

The objective of this research is to examine processing and chemistry modification effects on weld microstructures, and to correlate the cryogenic properties changes with these weld chemistry and microstructure changes.

## **EXPERIMENTAL PROCEDURE**

The composition of the base material is 18Mn-16.3Cr-5Ni-0.5Si-0.22N-0.024C-0.01S-0.004P. The 4 K longitudinal yield strength and L-T orientation fracture toughness of the base plate are 1140 MPa and 230 MPa-m<sup>1/2</sup>, respectively [8]. The 30 mm thick as-rolled plate was machined into 8 mm thick welding coupons.

Gas tungsten arc welding (GTAW) and electron beam welding (EBW) are used to examine heat input effects on weld microstructure and properties. Autogenous GTA welds are produced transverse to the rolling direction with argon backing gas on a water-cooled chill block using a pulsed-current mode. EB welds are also made transverse to the rolling direction. Welding parameters are shown in Table 1.

Controlled microalloying additions of N, Ni, and Mo are made to the welds in order to examine the effects of changing chemistry on the microstructure and properties. Nitrogen is added to the weld through the shield gas by metering N<sub>2</sub> through a flowmeter into the helium/argon shield gas flow stream. Ni and Mo additions to the GTA weld metal are made by spot welding high purity Ni or Mo strips to the base plate before welding.

Tensile tests are performed at both liquid nitrogen (77 K) and liquid helium (4 K) temperatures for an initial set of specimens. The composite specimen gage length contains both weld and base metal. Compact specimens are fatigue precracked at 77 K. The J<sub>IC</sub> tests are performed at 4 K under displacement control using a single specimen compliance technique to measure crack advance.

Interstitial nitrogen analysis is performed using a Leco gas analyzer. Specimens for nitrogen analysis are 1-mm thick through-thickness slices parallel to the centerplane of the weld, taken across the width of the weld. Substitutional solute analysis is obtained using EDX.

TEM foils from two orthogonal orientations are made by jet-polishing at 30-34 mA in a room temperature solution consisting of 75 gm Cr<sub>3</sub>O, 400 ml acetic acid, and 20 ml H<sub>2</sub>O. Fracture profile TEM specimens [16-18] are prepared from compact specimens tested at 4 K.

## RESULTS

### *Mechanical Properties*

The cryogenic yield and fracture toughness of the weldments are shown in Figure 1. With the exception of the high-N, Mo alloyed welds, these weldments necked and failed in the region between the weld centerline and the fusion boundary. Yielding initiated in the fusion zone. The composite tensile specimens with N and Mo additions failed in the heat affected zone.

Welds made with 75 vol% He - 25 vol% Ar shield gas mixture show a deterioration in mechanical properties at 4 K. EB welds show somewhat higher properties than the autogenous GTA welds. N-alloyed autogenous weldments show an improvement in 4 K yield strength. Weldments made with 75 vol% He - 25 vol% Ar and 3.46 wt-% Ni addition shows an improvement in toughness with some decrease in strength as compared to autogenous GTA welds.  $K_{Ic}$  values for Mo containing welds are generally lower than  $K_{Ic}$  values for welds not containing Mo. Mo addition appears to improve the retention of N in the weld (Table 3), increasing its 4 K yield strength.

The N content within the fusion zone differs significantly from that of the base metal (Fig. 2). The autogenous welds show a depletion of N in the fusion zone. Interstitial N concentration is 0.16 wt-% in the fusion zone, 27% lower than that of the base metal. EB welds made at two different travel speeds also show N depletion, with the average interstitial N content for both welds being 0.17 wt-%, slightly higher than that of the autogenous GTA welds.

The alloying element concentrations in welds are shown in Table 3. Welds made using shield gas containing  $N_2$  have higher average N content than that of the base metal. The N distributions in the fusion zones of these N-alloyed welds are nonuniform, reaching a maximum at the centerline of the fusion zone. Welds made with Ni addition but without  $N_2$  in the shield gas have an average N content lower than that of the welds made without Ni addition, 0.14 wt-% vs. 0.16 wt-%. The Mo containing welds made with N addition to the shield gas show a significantly higher N content within the fusion zone than that of welds made without Mo. The average N concentration within the Mo containing welds with 3 vol%  $N_2$  in the shield gas is 0.32 wt-% and with 6 vol%  $N_2$  is 0.35 wt-%.

Chemical composition profiles across dendrites of the autogenous welds show a depletion of Ni and an accumulation of Cr and Si in the dendrite core region. A similar profile for Mo-alloyed welds shows Mo in these regions. Conversely, an accumulation of Ni in the interdendritic region and a slight depletion of Cr and Mo are detected. This partitioning behavior is expected of welds solidifying in a primary ferrite mode.

### *Microstructure*

Examination of the 4 K fracture surfaces reveals that the fracture mode is predominantly ductile-microvoid coalescence, with some areas appearing more planar, less ductile. The dimple sizes for all GTA welds are qualitatively similar. The dimple sizes for the EB welds are

approximately an order of magnitude smaller than those of the GTA welds, with very few large inclusions visible (Fig. 3).

There was no significant variation in size distribution or content of inclusions among the various welds. Mean inclusion size is 0.5-1.0  $\mu\text{m}$  in diameter with very few inclusions of size greater than 1.0  $\mu\text{m}$ . Qualitative EDX chemical analysis performed on inclusions shows that these inclusions are predominantly MnS, with some Cr and Fe containing inclusions. Mo modified welds also have some Mo containing inclusions.

The fracture surface features of EB welds are qualitatively similar to those of the autogenous GTA welds. Both GTA and EB welds have relatively smooth, high aspect ratio features (Fig. 4). These features contain secondary ridges lying perpendicular to long primary ridges and are associated with the dendritic solidification structure. On the fracture surfaces of the autogenous GTA welds, the mean spacing between the ductile ridges is 6.6  $\mu\text{m}$ , while in the EB welds, the mean spacing is 3.1  $\mu\text{m}$ . These high aspect ratio features are larger and more continuous in the GTA welds than in the EB welds. The mean size of these features in the autogenous GTA welds are approximately 50x280  $\mu\text{m}$ , while in the EB welds, they are approximately 6x45  $\mu\text{m}$ . The areal fractions of the fracture surface covered by these features are similar in both GTA and EB welds. The areal fraction covered by these features is 20% in the autogenous GTA welds and 19% in the EB welds. Such features are not readily apparent on Ni-alloyed and N-alloyed weld fracture surfaces.

The N alloyed welds generally show a less ductile fracture appearance, with more planar dimple walls, showing less deformation as compared to the Ni alloyed and the autogenous weld samples (Fig. 5). Inclusions seen on the bottom of these dimples are generally spherical. Very few fractured inclusions are present, indicating void nucleation is primarily due to separation of the inclusions from the matrix. There are some relatively planar regions on the fracture surfaces of the high N welds (0.26 vol%) which show an extensive set of roughly parallel ridges spaced about 1  $\mu\text{m}$  apart (Fig. 6). These planar regions are similar in size to the grain widths of the welds and occupy approximately 9.8% of the fracture surface area.

Volume fractions of  $\delta$ -ferrite in the ferrite containing welds are listed in Table 6. The autogenous GTA weld metal has a generally continuous  $\delta$ -ferrite structure with 9.7 vol%  $\delta$ -ferrite content. Although EB welds also have the same type of structure, the  $\delta$ -ferrite is less continuous and the retained  $\delta$ -ferrite content lower (7.2 vol%), a consequence of its finer solidification substructure. The Ni alloyed welds have a more discontinuous  $\delta$ -ferrite structure (Fig. 7) than that of the autogenous welds and a lower  $\delta$ -ferrite content - 5.7 vol% near the weld centerline. Mo-alloyed welds also show a continuous  $\delta$ -ferrite structure (Fig. 8), but the amount of retained  $\delta$ -ferrite (18 vol%) and the continuity of the  $\delta$ -ferrite structure is higher than that of the autogenous welds. Welds alloyed with both Mo and N also contain continuous retained  $\delta$ -ferrite, but the total amount retained (13 vol%) is closer to that of the autogenous weld. The N-alloyed welds appear  $\delta$ -ferrite free near the centerline, but a  $\delta$ -ferrite containing layer is evident at the fusion boundary. All GTA welds have similar primary dendrite arm widths and secondary arm spacings while the lower heat input EB weld substructures are smaller.

TEM observations reveal no evidence of precipitates in these welds. However the N-alloyed weld metal contain small ( $< 0.5 \mu\text{m}$  diameter), discrete, ferrite particles near the the weld centerline, primarily in the interdendritic regions. This suggests that the weld solidifies as primary austenite, and that the ferrite particles form in the Cr rich interdendritic regions. The 4 K deformation of base and N-alloyed welds is inhomogeneous, concentrated in intense bands on certain (111) planes (Fig. 9).

## DISCUSSION

### *Yield Strength*

GTA and EB weld metal 4 K yield strengths are significantly lower than those of base metal, 1040 MPa for the autogenous GTA, 1040 and 1060 for the two EB welds, as compared to 1140 MPa for base metal. This decrease is attributed to N loss. The cryogenic yield strength of austenitic alloys, this alloy in particular, is strongly dependent on their interstitial N content [6,7,19]. The steep N chemical potential gradient between the molten fusion zone and the N free shield gas causes N diffusion away from the molten fusion zone into the shielding atmosphere. The molten metal solidifies in its N depleted state, resulting in the decreased yield strength of the as-solidified material. The composition profile shows a decreasing N content across the fusion zone: 0.22 wt-% in the base metal falling to 0.16 wt-% within the fusion zone, a 27% decrease. EB welds show a similar decrease in interstitial N content; the average N concentration within the fusion zone is 0.17 wt-%.

Use of N-containing shield gas has been effective in increasing interstitial N in Fe-Cr-Ni austenitic alloy weldments [20-22]. The N content of welds made with N additions to the shield gas is shown in Figure 10. The average weld N content increases as shield gas N content increases, saturating at 6 vol% N shield gas at 0.26 wt-%. The increased weld N content results in increased weldment yield strength.

The additions of substitutional solute species, used to control the amount of ferrite in the as-solidified weld region, also affect the yield strength of the weldment. The primary effect of Ni addition is expected to be on toughness [12]. Since the lattice distortion due to Ni is small [23], its impact on yield strength should be small. However, Ni addition also decreases the level of N retained in the fusion zone. A 3.5 wt-% Ni addition results in a N level of 0.14 wt-% for the welds made with 75 vol% He - 25 vol% Ar, compared with 0.16 wt-% for autogenous welds, a 13% decrease. This decrease in N content causes a drop in the weld yield strength, from 1040 MPa for autogenous GTA to 960 for Ni-alloyed.

Conversely, Mo addition increases the yield strength level. The Mo effect on yield strength is two-fold: an increase due to significant lattice distortion caused by the larger Mo atomic size [40], and an increase accompanying increased dissolved N content. The solute strengthening effect of Mo in Fe-Cr-Ni austenite is approximately 20 MPa/at% at 293K [24], increasing to 100 MPa/at% at 4 K [25]. In the welds, with a 0.58 wt-% Mo addition the yield strength is 1080 MPa for welds made with 75 vol% He - 25 vol% Ar shield gas, in contrast to a yield strength of 1040 MPa for autogenous welds. These Mo-alloyed welds show a slight

decrease in average N content, 0.15 wt-% as compared to 0.16 wt-% for autogenous welds. This is due to the increased retention of  $\delta$ -ferrite. Mo is a strong ferrite stabilizing element [10,24], and the welds containing Mo have a  $\delta$ -ferrite content of 18 vol%. The greatly reduced solubility of N in ferrite accounts for the lower weld N content. The presence of a higher volume fraction of  $\delta$ -ferrite or a lower volume fraction of austenite will result in a lower measured average N content within the fusion zone. However, the addition of N through the shield gas decreases the volume fraction of retained ferrite, and the level of retained N in the weld will increase. This is reflected in the yield strengths of Mo alloyed welds made with N additions to the shield gas. Welds made with Mo addition and 3 vol% nitrogen addition to the shield gas mixture have an average N content of 0.32 wt-% and a yield strength of 1145 MPa, a significant increase compared to the yield strengths of the autogenous and Mo-alloyed welds of 1040 MPa and 1080 MPa, respectively.

The yield strength decrease on welding cannot be attributed solely to changes in interstitial N content. Even weld metal with average interstitial N content greater than that of the base metal is not able to achieve the yield strength level of the base metal (Fig. 1i). Therefore, the altered microstructure must also affect the yield strength of the welds. The as-solidified weld metal microstructure is coarser than that of the base metal and therefore has lower yield strength than the base metal. This is seen in the slightly lower yield strength of autogenous GTA weldments as compared to the higher yield strength EB weldments, which, because of lower heat input and narrow fusion zones, have higher cooling rates and thus a finer as-solidified microstructure. Since the N contents in both GTA and EB welds are similar, most of the difference in yield strength must be attributed to the differences in microstructure. The finer as-solidified microstructure of the EB welds results in somewhat higher yield strength.

The as-solidified weld metal is inhomogeneous. Both chemical composition and grain size and shape vary from point to point within the welds. Thus it is difficult to quantitatively separate microstructural and chemical effects on yield strength. However, qualitatively, grain size has a smaller impact on yield strength than interstitial N content. The 50% decrease in grain size of the EB welds as compared to GTA welds raises the yield strength only 20 MPa. A 50% increase in the interstitial N content results in a 100 MPa increase in yield strength. Chemistry effects thus dominate. Compensation for N depletion can improve weldment yield strength more effectively than changes in microstructure via changes in heat input.

### *Fracture Toughness*

The fracture toughness of the high-manganese weldments is significantly lower ( $\leq 60 \text{ MPa}\cdot\text{m}^{1/2}$ ) than that of the base metal. High inclusion contents, leading to high microvoid nucleation site densities, can lead to low fracture toughness in a ductile-transgranular fracture mode. The fracture mode of welds in this study is primarily ductile-transgranular. The inclusions seen at the bottom of the dimples on the fracture surfaces are Mn sulfide with some Cr and Fe containing inclusions which may be oxides. Few fractured inclusions are observed; most of the observed inclusions are intact and spherical. Void nucleation is thus primarily due to decohesion of the spherical inclusions from the matrix. Measured inclusion densities are within a narrow range for all weldments - GTA autogenous, Ni-, N-, and Mo-alloyed. The 4 K fracture toughness shows no correlation with the inclusion contents of these



welds. The observed variations in the fracture toughness of weld specimens (autogenous, N-, Ni-, and Mo-alloyed) is thus not attributable to the differences in inclusion contents.

The presence of non-austenite phases, specifically  $\delta$ -ferrite, is detrimental to the cryogenic fracture toughness of welds. Regions of  $\delta$ -ferrite can act as crack initiation sites, and long continuous  $\delta$ -ferrite structures serve as easy crack propagation paths at cryogenic temperatures in Fe-Ni-Cr austenitic steels. Charpy impact tests of 300 series shielded metal arc (SMA) weld metal at temperatures down to 77 K indicate that weld metal cryogenic toughness varies inversely with ferrite content; maximum notch toughness is attained for fully austenitic weld metals [13,15]. A similar inverse dependence is observed for fracture toughness at 4 K [15].

Measurements of  $\delta$ -ferrite on polished and etched cross sections of the autogenous GTA weld indicate a 9.7 vol%  $\delta$ -ferrite content. The  $\delta$ -ferrite has a semicontinuous morphology and is located at the dendrite core, indicative of solidification as primary ferrite with subsequent transformation to austenite. The  $\delta$ -ferrite-dendrite mean secondary arm spacing of the autogenous welds is 6.8  $\mu\text{m}$ .

The ferrite structure seen in the metallographic specimens can be correlated to features observed on the fracture surfaces. There are areas on the fracture surface which are associated with the solidification substructure, with short secondary ridges branching off perpendicular to long primary ridges. These regions appear smoother than the surrounding dimpled areas (Fig. 3). Measurements of the spacing between the secondary ridges indicate a mean spacing of 6.6  $\mu\text{m}$ . This closely correlates with that of the dendrite secondary arm spacing measured on the metallographic section, 6.8  $\mu\text{m}$ . The width of the primary dendrite arms on the fracture surfaces also correlates well with the width of the features on the metallographic section. This implies that the  $\delta$ -ferrite dendrites seen on the optical specimens correspond to the elongated relatively smooth features seen on the fracture surface.

The features associated with  $\delta$ -ferrite occupy 20 areal percent of the fracture surface, the remaining areas are covered with microvoids. The higher fracture-surface area fraction occupied by these features, as compared with that measured in the bulk, indicates that the crack has advanced preferentially along  $\delta$ -ferrite containing regions within the weld. The crack tends to advance along the direction of the primary arms of the dendrites as indicated by the high aspect ratio of  $\delta$ -ferrite associated features on the fracture surfaces. The grain growth direction near the weld centerline, for the low travel speeds used in making these welds, is aligned with the weld centerline. The crack therefore preferentially propagates through the  $\delta$ -ferrite regions until it encounters an austenite region, where propagation is via microvoid nucleation and coalescence. Thus processing variables such as heat input and travel speed, which influence the solidification substructure of the weld, have an effect on the cryogenic fracture toughness.

All  $\delta$ -ferrite containing welds show reductions in 4 K fracture toughness as compared to that of the base metal. The 4 K fracture toughness is inversely related to  $\delta$ -ferrite content (Fig. 12), a behavior similar to that observed for Fe-Cr-Ni austenitic weld metal [14]. The observed fracture toughness reduction can be directly correlated to the easy crack propagation paths through  $\delta$ -ferrite containing regions of the weld microstructure.

Further evidence of the deleterious effects of  $\delta$ -ferrite on cryogenic fracture toughness is seen in the Mo-alloyed welds. The addition of Mo, a ferrite stabilizing element, to the weld metal increases the  $\delta$ -ferrite content to 18 vol% for a 0.58 wt-% Mo addition. The  $\delta$ -ferrite morphology is similar to that in the autogenous welds, but it is coarser and more continuous in the Mo-alloyed welds (Fig. 8). The areal fraction occupied by  $\delta$ -ferrite regions on the Mo-alloyed weld fracture surface is 32%. This increase in  $\delta$ -ferrite content and its continuous nature is reflected in the concomitant decrease in 4 K fracture toughness as compared to that of the autogenous welds, 115 MPa-m<sup>1/2</sup> as opposed to 150 MPa-m<sup>1/2</sup>. This is further evidence that the preferred crack propagation path is through the  $\delta$ -ferrite regions.

Ni addition has the opposite effect on the retained  $\delta$ -ferrite content of the welds. A 3.5 wt-% Ni addition to the weld metal decreases the retained  $\delta$ -ferrite content to 5.7 vol%. The increased Ni content destabilizes the retained  $\delta$ -ferrite, leading to a more fragmented  $\delta$ -ferrite structure. No  $\delta$ -ferrite associated features are found on the fracture surface. A less continuous  $\delta$ -ferrite structure and the lower overall  $\delta$ -ferrite content results in fewer crack nucleation sites, less continuous crack propagation paths, and consequently an improved fracture toughness. The fracture toughness improvement, however, cannot be solely attributed to decreased  $\delta$ -ferrite content. The increased Ni content decreases the amount of retained N in the weld metal, lowering the yield strength. Although there may be an increase in fracture toughness due to the lower yield strength, the amount is small since the yield strength change is itself relatively small.

N addition also significantly affects the microstructure of the weld metal. An average interstitial N content of 0.24 wt-% results in a microstructure which is almost ferrite free near the weld centerline, with some ferrite retained in the weld metal near the fusion boundary. Similar microstructures are seen in the 0.26 wt-% N content welds. TEM observations indicate that ferrite is present in the form of small (less than 0.5  $\mu$ m in diameter) discrete particles at the interdendritic regions near the centerline of these welds, suggesting that these welds solidified as primary austenite with the Cr rich, Ni depleted interdendritic regions becoming ferrite. The small size and discrete nature of ferrite particles in these welds suggest that ferrite does not play a significant role in determining the fracture toughness of these welds; they should behave more like inclusions. However, the fracture toughness of N-alloyed welds is not higher than  $\delta$ -ferrite containing autogenous welds. Yield strength, inclusion content, and  $\delta$ -ferrite effects on fracture toughness are not significant in these N-alloyed welds, so intrinsic factors such as the deformation behavior must be operating.

In addition to its effect on phase stability, chemistry also has an effect on the intrinsic deformation behavior of the material. These effects may dominate in the large grain microstructure of the weld metal at cryogenic temperatures. The grains are large and highly directional due to the competitive growth process which occurs during solidification [11]. Nitrogen is used as an interstitial strengthening element in this alloy. High N Fe-Cr-Ni stainless steels are known to deform in an inhomogeneous mode [26]. This is due to the low stacking fault energies of these steels, inhibiting the cross-slip required for homogeneous deformation [27]. It has also been suggested that planar slip concentrated in bands as seen in these materials can be due to formation of short-range order zones within the material [28]. This inhibits slip until applied stress is sufficient to cause some zones to shear, disrupting order, and al-

lowing further slip to proceed easily on the same planes. The deformation is then concentrated in those planes. Such localized deformation lowers fracture toughness by limiting strain accommodation to a smaller effective volume leading to higher local stresses for a given macroscopic strain. Modeling of dislocation motion mechanics predicts inhomogeneous slip at low temperatures [30]. Inhomogeneous deformation effects are expected to become dominant as grain size increases: dislocation pileups at matrix discontinuities can be built up over longer distances, resulting in higher local stresses at a given macroscopic strain, leading to premature cracking or void nucleation and lower fracture toughness.

Inhomogeneous deformation behavior is observed in the N-alloyed welds. Their fracture surfaces contain planar regions with numerous closely spaced parallel ridges (Fig. 6). The mean size of these regions is approximately that of the grain widths. The ridge spacing is qualitatively similar to the spacing between slip bands seen in deformed weld metal specimens with TEM (Fig. 9). This suggests that the ridges are manifestations of slip bands on the fracture surface. Similar features, believed to be slip band traces appearing on  $\gamma(111)$  cleavage planes, have been observed on the fracture surfaces of high-Mn, high-N base metal tested at cryogenic temperatures [9,29]. This deformation behavior may be related to the lower than expected fracture toughness of the N-alloyed welds.

## CONCLUSIONS

The 4 K yield and fracture toughness of N-strengthened-high-Mn alloys both degrade on welding. Yield strength degradation is primarily due to N loss from the fusion zone and can be partially controlled by increasing N in the fusion zone through additions to the shield gas in GTA welds. Chemical modifications to the weld are more effective in controlling the yield strength than grain size changes. Ni added to control  $\delta$ -ferrite levels in the weld causes a decrease in the amount of retained N. This leads to a lower weld yield strength: 960 MPa for the Ni-alloyed vs. 1040 MPa for the autogenous. Conversely, Mo-alloying addition when used with N-containing shield gas increases the retained N level significantly, thus increasing the yield strength level.

Weld fracture toughness is lower than base metal fracture toughness. Fracture toughness degradation is attributed to two competing mechanisms. Retained  $\delta$ -ferrite is the primary cause of the fracture toughness loss in the low N autogenous welds. Fracture toughness in autogenous, Ni-, and Mo-alloyed welds is shown to be inversely related to  $\delta$ -ferrite content. Crack propagation in  $\delta$ -ferrite containing welds is solidification substructure specific. Fracture surface features of  $\delta$ -ferrite containing welds have been correlated with the  $\delta$ -ferrite regions. These  $\delta$ -ferrite containing regions are preferred crack propagation paths. Processing which breaks up the  $\delta$ -ferrite substructure (low heat input EBW) and reduces  $\delta$ -ferrite content increases fracture toughness. Ni additions, which decrease  $\delta$ -ferrite content and fragments the  $\delta$ -ferrite, is also effective in raising fracture toughness. The high-N welds, which contain only traces of ferrite, have fracture toughness values similar to  $\delta$ -ferrite containing welds. The unexpectedly low fracture toughness of these austenitic welds is associated with the appearance of inhomogeneous deformation behavior in these high-N-high-Mn austenitic steels.

## ACKNOWLEDGEMENT

B. L. Olsen of the Lawrence Livermore National Laboratory made the EB welds used in this study. This work is supported by the Director, Office of Energy Research, Office of Fusion Energy, Development and Technology Division of the U. S. Department of Energy under Contract No. DE-AC03-76SF00098.

## REFERENCES

1. Yoshida, K., H. Nakajima, et. al., "Development of Cryogenic Structural Materials for Tokamak Reactors," Austenitic Steels at Low Temperatures, New York, Plenum Press, pp. 29-39.
2. Nakajima, H. et al., "Mechanical Properties of Welded Joints of the New Cryogenic Steel," Presented at the 5<sup>th</sup> Cryogenic Structural Materials Workshop, Reno, NV, October 6-8, 1986.
3. McHenry, H. I. and R. P. Reed, "Structural Alloys for Superconducting Magnets in Fusion Energy Systems," Nuclear Engineering and Design, 58, 1980, pp.219-236.
4. McHenry, H. I., "Strength and Toughness Goals for Cryogenic Steels," Materials Studies for Magnetic Fusion Energy Applications at Low Temperatures - VIII, NBSIR 85-3025, 1985.
5. Ogawa, R. and J. W. Morris, Jr., The Cryogenic Mechanical Properties of High Manganese Austenitic Stainless Steels, LBL-21933, July 1986.
6. Horiuchi, T., R. Ogawa, and M. Shimada, "Cryogenic Fe-Mn Austenitic Steels," Advances in Cryogenic Engineering - Materials, 32, 1986, pp. 33-42.
7. Ogawa, R. and J. W. Morris, Jr., "The Influence of Alloy Composition on the Cryogenic Mechanical Properties of AISI 200 Grade High Manganese Austenitic Steels," Proceedings of the ICMC, Kobe Japan, May 1983, pp. 214-218.
8. Ogawa, R. and J. W. Morris, Jr., The Influence of Processing on the Cryogenic Mechanical Properties of High Strength High Manganese Stainless Steel, LBL-16528, August 1983.
9. Strum, M. J., Control of Cryogenic Intergranular Fracture in High-Mn Austenitic Steels, Ph.D. Thesis, U. C., Berkeley, 1986.
10. Pickering, F. B., "Physical Metallurgy of Stainless Steel Developments," International Metals Reviews, 21, December 1976, pp. 227-268.
11. Sakamoto, T., Y. Nakagawa, and I. Yamauchi, "Effect of Mn on the Cryogenic Properties of High Nitrogen Austenitic Stainless Steels," Advances in Cryogenic Engineering - Materials, 32, 1986, pp. 65-72.
12. Delder, E. N. C. and M. C. Juhas, Austenitic Stainless Steels for Cryogenic Service, UCRL-92882, September 1985.

13. Witherell, C. E., "Welding Stainless Steels for Structures Operating at Liquid Helium Temperature," Welding Journal, 59, no. 11, November 1980, pp. 326s-342s.
14. Read, D. T., et al., "Metallurgical Factors Affecting the Toughness of 316L SMA Weldments at Cryogenic Temperatures," Welding Journal, 59, no. 4, April 1980, pp. 104s-113s.
15. Szumachowski, E. R. and H. F. Reid, "Cryogenic Toughness of SMA Austenitic Stainless Steel Weld Metals: Part 1 - Role of Ferrite," Welding Journal, 57, no. 11, November 1978, pp. 325s-333s.
16. Hogmark, S., H. Swahn, O. Vingsbo, "A Specimen Preparation Technique for Transmission Electron Microscopy of Surface Layers," Ultramicroscopy, 1, 1975, pp. 113-120.
17. Jin, S., J. W. Morris, Jr., et. al., "An Investigation of Transformation Strengthening in Precipitation-Hardened Fe-Ni Austenite," Metallurgical Transactions A, 9A, November, 1978, pp. 1625-1633.
18. Kim, Y.-H., H. J. Kim, and J. W. Morris, Jr., "The Influence of Precipitated Austenite on Hydrogen Embrittlement in 5.5 Ni Steel," Metallurgical Transactions A, 17A, July 1986, pp. 1157-1164.
19. Reed, R. P. , P. T. Purtscher, and K. A. Yushchenko, "Nickel and Nitrogen Alloying Effects on the Strength and Toughness of Austenitic Stainless Steels at 4 K," Advances in Cryogenic Engineering - Materials, 32, 1986, pp. 43-50.
20. Cieslak, et al., "Solidification Cracking and Analytical Electron Microscopy of Austenitic Stainless Steel Weld Metals," Welding Journal, 61, January 1982, pp. 1s-8s.
21. Baeslack, W. A, Savage, W. F., and Duquette, D. J., "Effect of Nitrogen on Microstructure and Stress Corrosion Cracking of Stainless Steel Weld Metals," Welding Journal, 58, no. 3, March 1979, pp. 83s-90s.
22. Okagawa, R. K., R. D. Dixon, and D. L. Olson, " The Influence of Nitrogen from Welding on Stainless Steel Weld Metal Microstructures," Welding Journal, 62, no. 8, August 1983, pp. 204s-219s.
23. Irvine, K. J., et al., "High-Strength Austenitic Stainless Steels," Journal of Iron Steel Institute, 199, 1961, pp. 153-175.
24. Marshall, P., Austenitic Stainless Steels Microstructure and Mechanical Properties, New York, Elsevier Applied Science Publishing Co, 1984.
25. Yamamoto, S., N. Yamagami, and C. Ouchi, "Effect of Metallurgical Variables on Strength and Toughness of Mn-Cr and Ni-Cr Stainless Steels at 4.2 K," Advances in Cryogenic Engineering - Materials, 32, 1986, pp. 57-64.
26. Swann P. R., "Dislocation Substructure vs. Transgranular Stress Corrosion Susceptibility of Single Phase Alloys," Corrosion, 19, no. 3, March 1963, pp. 102t-112t.

27. Schramm, K. E. and R. P. Reed, "Stacking Fault Energies of Seven Commercial Austenitic Stainless Steels," Metallurgical Transactions A, 6A, July 1975, pp. 1345-1351.
28. Douglass, D. L., et al., "Ordering, Stacking Faults and Stress Corrosion Cracking in Austenitic Alloys," Corrosion, 20, no. 1, January 1964, pp. 15t-28t.
29. Tobler, R. L. and D. Meyn, "Cleavage-like Fracture in Fe-18Cr-3Ni-13Mn-0.37N Austenitic Stainless Steel at Liquid Helium Temperature," Materials Studies for Magnetic Fusion Energy Applications at Low Temperatures - VIII, NBSIR 85-3025.
30. Altintas, S., K. Hanson, and J. W. Morris, Jr., "Computer Simulation of Plastic Deformation Through Planar Glide in an Idealized Crystal," Journal of Engineering Materials and Technology, 98, January 1976, pp. 86-91.

Figure captions

- Figure 1. Weld 4 K fracture toughness as a function of yield stress. The line is the strength-toughness behavior for welds with varying N content.
- Figure 2. N profile across an autogenous GTA weld.
- Figure 3. SEM fractographs of a) autogenous GTA and b) EB weld compact specimens tested at 4 K.
- Figure 4. SEM fractographs of a) autogenous GTA and b) EB weld compact specimens tested at 4 K showing features associated with the solidification substructure.
- Figure 5. SEM fractographs of a) autogenous, b) 8.42 wt-% Ni-alloyed, and c) 0.24 wt-% N-alloyed GTA weld compact specimens tested at 4 K.
- Figure 6. SEM fractographs of 0.26 wt-% N-alloyed GTA weld compact specimens tested at 4 K showing the appearance of ductile ridges on relatively planar areas.
- Figure 7. Optical micrograph of an 8.42 wt-% Ni-alloyed GTA weld. The dark discontinuous phase is ferrite.
- Figure 8. Optical micrographs of a) 0.58 wt-% Mo-alloyed and b) autogenous GTA welds. Ferrite appears in relief.
- Figure 9. Bright-field TEM micrograph of 0.26 wt-% N-alloyed weld deformed at 4 K. The dark bands are overlapping dislocations and stacking faults.
- Figure 10. Average fusion zone N content as a function of shielding gas N<sub>2</sub> content.
- Figure 11. 4 K yield strength as a function of average fusion zone N content.
- Figure 12. 4 K fracture toughness as a function of ferrite content.

Table 1: Welding parameters.

<u>Parameter</u>	<u>GTA</u>	<u>EB</u>
Current:		22 mA
Pulse:	150-185 A	
Background:	80-100A	
Duty cycle:	75%	
Voltage:	19 V	115 kV
Travel speed:	51 mm/min	510 mm/min 760 mm/min
Shielding gases:	75% He & 25% Ar 75/25 + 1 vol% N <sub>2</sub> 3 vol% N <sub>2</sub> 6 vol% N <sub>2</sub>	
Backing gas:	Ar	
Vacuum:		2x10 <sup>-4</sup> Torr
Electrode:	2.38 mm dia., 60° tip	
Arc gap:	2 mm	



**Table 2. Fusion zone content of the major alloying elements in wt-%.**

<b>Process</b>	<b>Alloying addition</b>	<b>Mn</b>	<b>Cr</b>	<b>Ni</b>	<b>N</b>	<b>Mo</b>
<b>EB</b>	--	<b>18.85</b>	<b>16.14</b>	<b>4.87</b>	<b>0.17</b>	--
<b>GTA</b>	--	<b>18.59</b>	<b>15.19</b>	<b>4.97</b>	<b>0.16</b>	--
	<b>Ni</b>	<b>18.80</b>	<b>15.00</b>	<b>8.42</b>	<b>0.14</b>	--
	<b>3 vol% N<sub>2</sub></b>	<b>18.58</b>	<b>15.18</b>	<b>4.91</b>	<b>0.24</b>	--
	<b>6 vol% N<sub>2</sub></b>	<b>18.60</b>	<b>15.21</b>	<b>4.98</b>	<b>0.26</b>	--
	<b>Mo</b>	<b>18.76</b>	<b>15.16</b>	<b>5.01</b>	<b>0.15</b>	<b>0.58</b>
	<b>Mo+3 vol % N<sub>2</sub></b>	<b>18.43</b>	<b>15.18</b>	<b>5.17</b>	<b>0.32</b>	<b>0.47</b>

**Table 3. Fracture surface and bulk ferrite content.**

	GTA						EB
Alloying addition	Mo	Mo+3N <sub>2</sub>	--	Ni	3N <sub>2</sub>	6N <sub>2</sub>	--
Bulk	18	13	9.7	5.7	<2	<2	7.2
Fracture surface	32	20	20.6	--	--	--	19.2

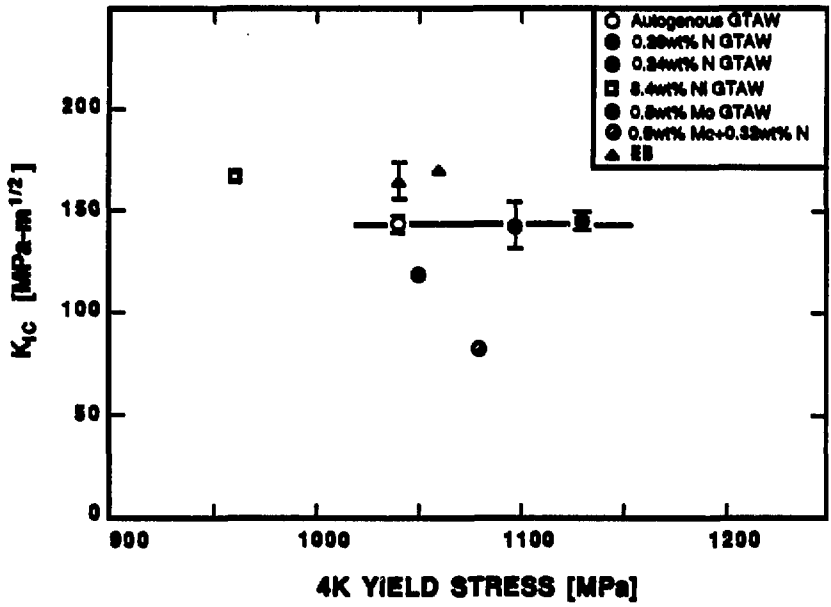
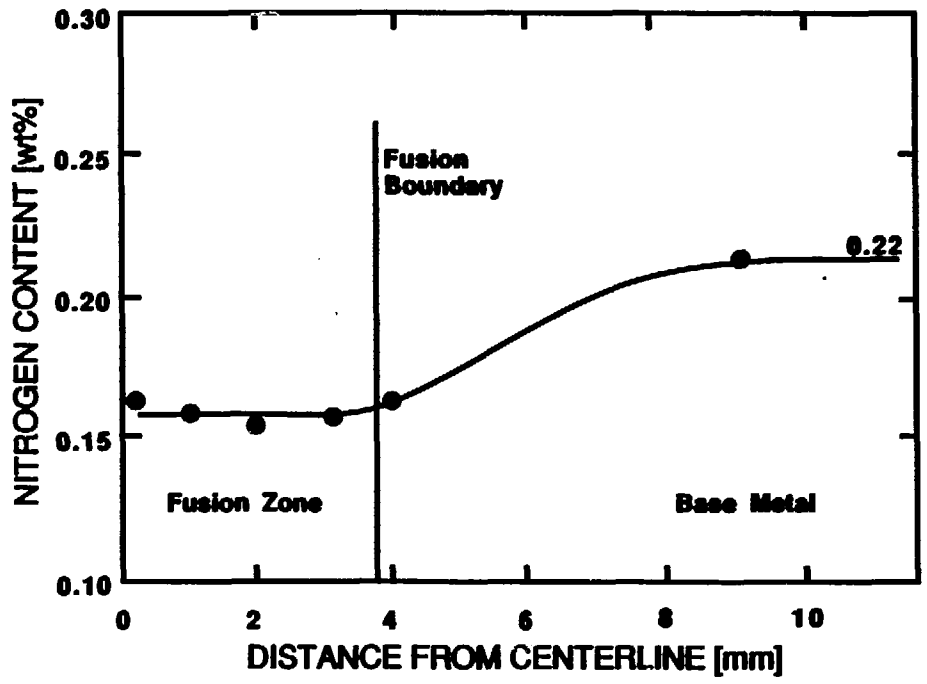


Figure 1

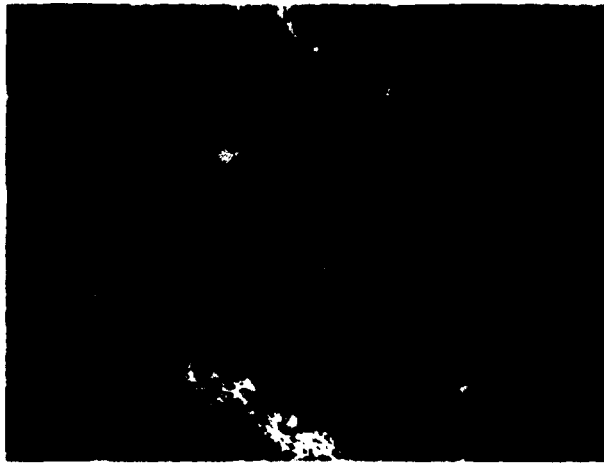
Figure 2





10 $\mu$ m

(a)

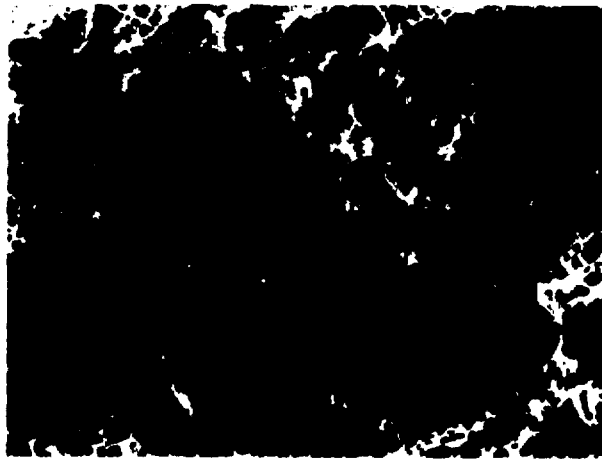


10 $\mu$ m

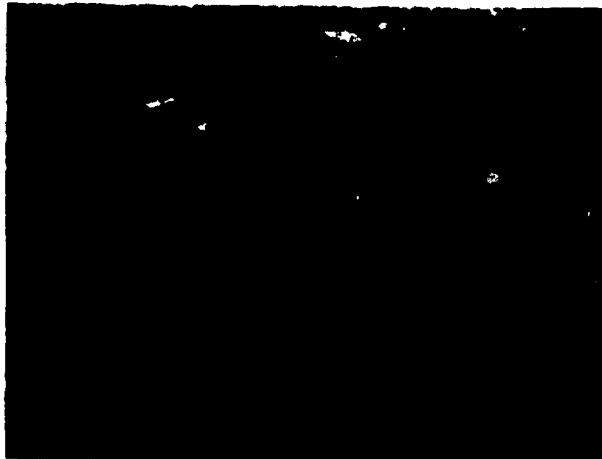
(b)

XBB860-10234

Figure 3



(a)



(b)

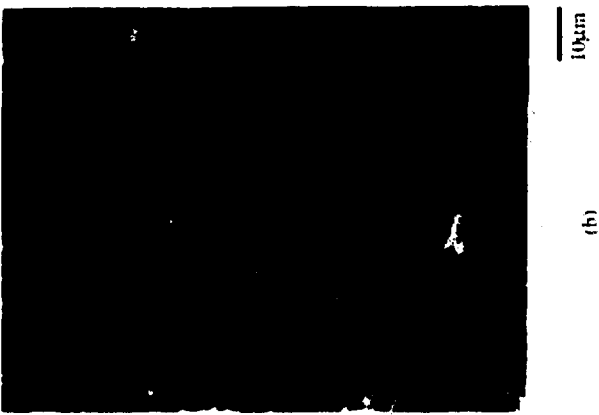
XBB 860-10232

Figure 4



10µm

(c)



10µm

(b)

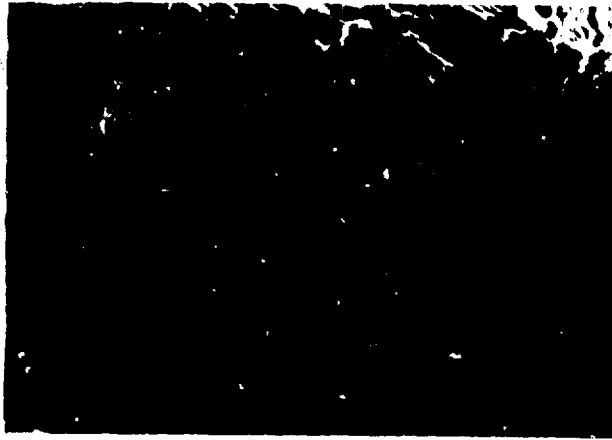


10µm

(a)

XBB 860-10228

Figure 5



(a)

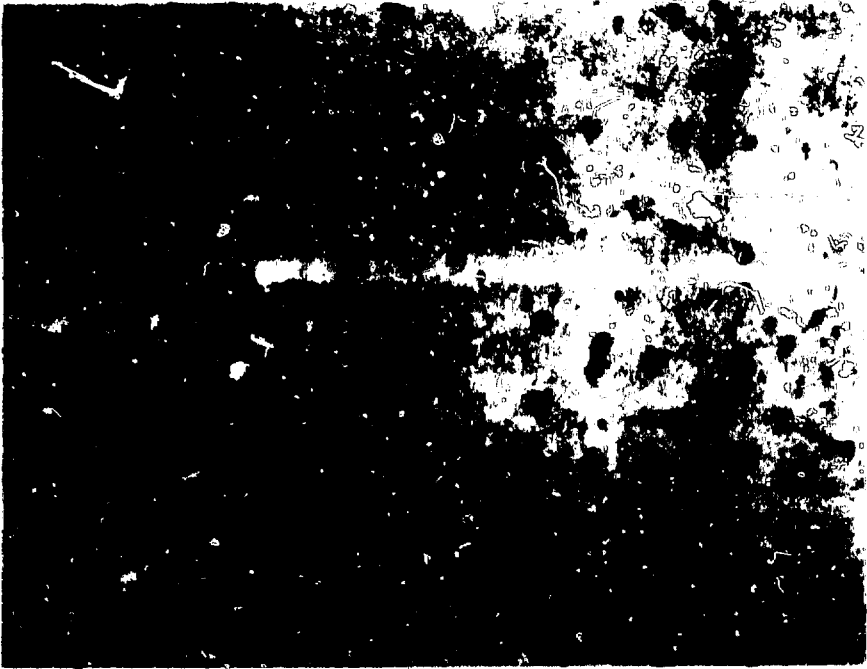


(b)

ZBB 860-10233

Figure 6





10 $\mu$ m

XBB 860-10226

Figure 7



100µm

(a)



100µm

(b)

XBB 860-10230

Figure 8



0.25 μm

XBB 875-3835

Figure 9

Figure 10

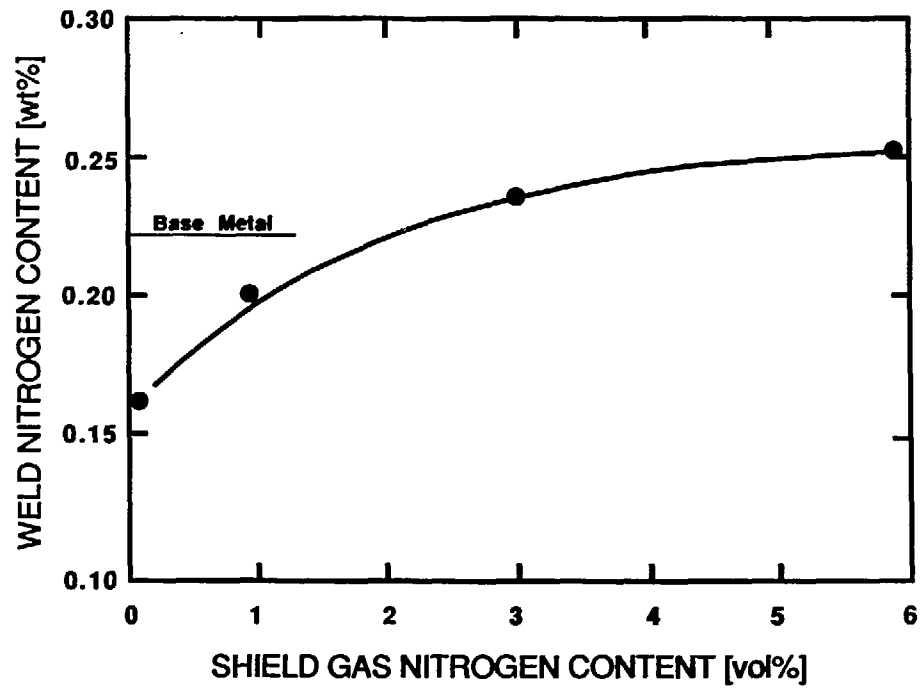
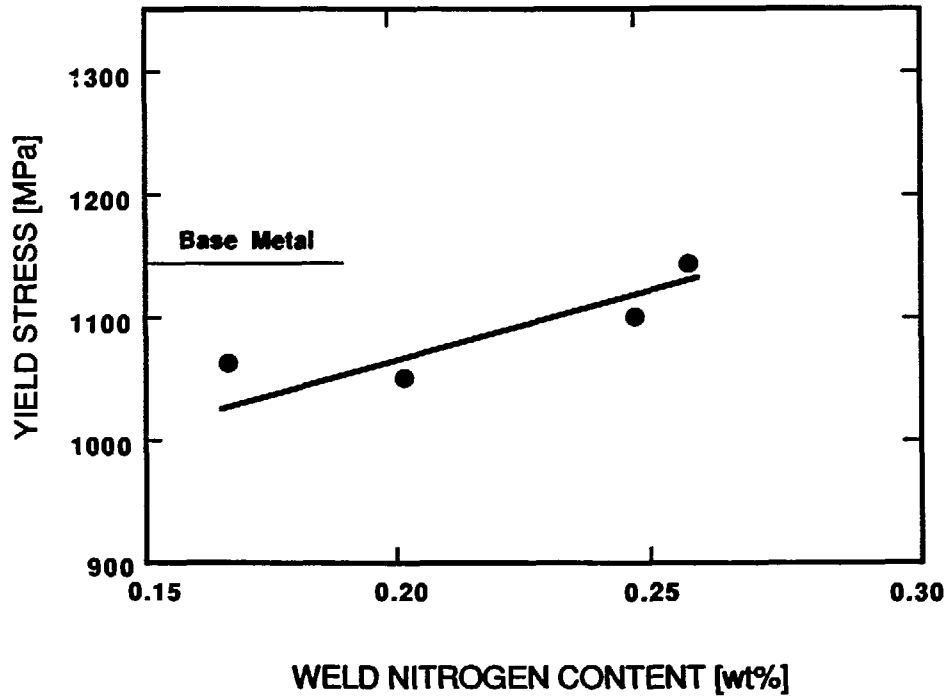


Figure 11



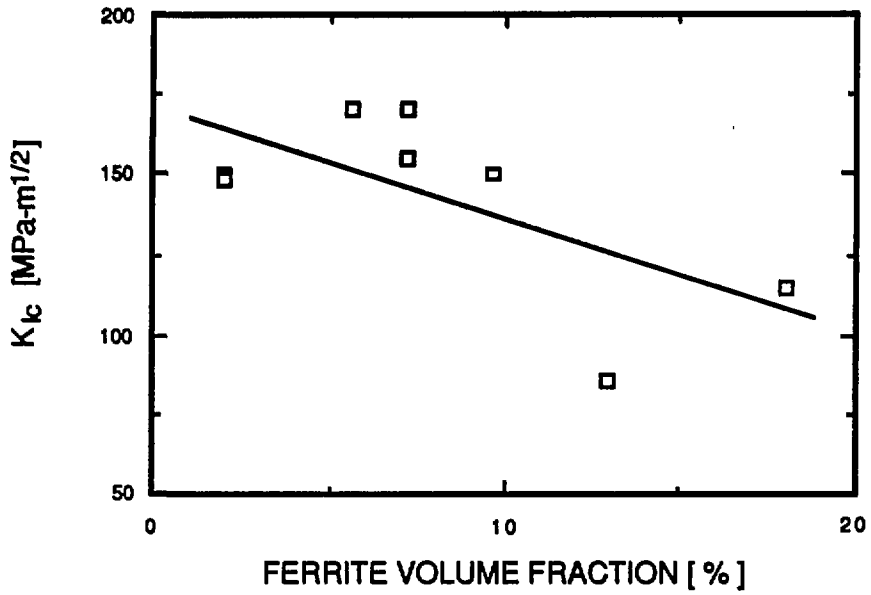


Figure 12